Evolution of load transfer between hydroxyapatite and collagen during creep deformation of bone

A.C. Deymier-Black [a,*], F. Yuan [a], A. Singhal [a], J.D. Almer [b], L.C. Brinson [a,c], D.C. Dunand [a]

[a] Department of Materials Science & Engineering, Northwestern University, Evanston, IL 60208, USA
[b] Advanced Photon Source, Argonne National Laboratory, Argonne, IL 60439, USA
[c] Department of Mechanical Engineering, Northwestern University, Evanston, IL 60208, USA

ARTICLE INFO

ABSTRACT

While the matrix/reinforcement load-transfer occurring at the micro- and nanoscale in nonbiological composites subjected to creep deformation is well understood, this topic has been little studied in biological composites such as bone. Here, for the first time in bone, the mechanisms of time-dependent load transfer occurring at the nanoscale between the collagen phase and the hydroxyapatite (HAP) platelets are studied. Bovine cortical bone samples are subjected to synchrotron X-ray diffraction to measure in situ the evolution of elastic strains in the crystalline HAP phase and the evolution of viscoelastic strains accumulating in the mineralized collagen fibrils under creep conditions at body temperature. For a constant compressive stress, both types of strains increase linearly with time. This suggests that bone, as it deforms macroscopically, is behaving as a traditional composite, shedding load from the more compliant, viscoelastic collagen matrix to the reinforcing elastic HAP platelets. This behavior is modeled by finite-element simulation carried out at the fibrillar level.

© 2011 Acta Materialia Inc. Published by Elsevier Ltd. All rights reserved.

1. Introduction

Calcified tissues such as bone are highly complex composite materials with remarkable properties (such as light weight, high toughness and high strength) made possible by their unique composition and hierarchical architecture [1]. Bone is a three-phase composite consisting of an inorganic mineral component, hydroxyapatite (HAP), a polymeric or proteinaceous component, collagen, and fluid-filled porosity. The HAP and collagen combine to form the basic building block of bone, the mineralized fibril. These fibrils are the main components in the lamellae which constitute the bulk of osteons. Cortical bone also contains haversian canals and lacunae, which are responsible for its fluid-filled porosity.

Many of the macroscopic properties of calcified biological materials—e.g. elastic modulus, proportional limit, toughness and viscoelastic behavior—have been investigated in the bulk (e.g. by compressive testing [2–5] and ultrasonic measurements [6–8]) or over smaller volumes (e.g. by indentation and nanoindentation [9–12]). Some of these macroscopic studies have shown that bone undergoes creep deformation and stress-relaxation behaviors [13–15]. Bulk experiments, however, do not provide information about the relative contribution of the phases to the macroscopic creep behavior of bone, where temperature- and time-dependent

strain accumulates in the material. Rimnac et al. [15] have suggested that the collagen is not responsible for creep which is instead attributed to dislocations in the HAP mineral. Conversely, other researchers [14,16] have suggested that collagen is solely responsible for the creep of bone. These studies claim that creep within the HAP phase is unrealistic at the low stress and low temperatures usually employed for testing and hypothesize that the known deformation and sliding of collagen fibrils observed in unmineralized tendon is the cause of bone creep [17,18]. These discrepancies in the existing literature suggest a need for further studies using techniques that allow in situ quantification of the response of the different bone phases during loading to determine their contribution to the overall creep behavior of bone.

One such experimental technique, synchrotron X-ray diffraction, has been widely used to study the transfer of load from two different crystalline phases (matrix and reinforcement) in nonbiological composites such as metal matrix composites [19–21]. More recently, it has also been used to determine the load-transfer behavior of HAP and protein in bone and dentin under quasi-static loading conditions without creep [22–26]. Diffraction has also been used to determine the viscoelastic behavior of collagen in unmineralized tendon [27–29]. However, to date, this method has not been employed to determine the evolution of load partitioning among these phases in bone (or dentin and enamel) during creep loading. Such testing will help to determine how HAP and collagen interact during creep deformation and shed light on the role, if any, of HAP elastoplastic deformation and collagen fibril viscoelastic

* Corresponding author. Tel.: +1 847 491 5933; fax: +1 847 491 7820.
E-mail address: Alixdeymier2010@u.northwestern.edu (A.C. Deymier-Black).

sliding. Furthermore, knowledge about the behavior of healthy bone and its different phases under creep conditions at body temperature will shed light on creep behavior in damaged or diseased bone, as well as address the issue of creep at stress concentrations in bones (e.g. at crack tips, near damaged or diseased regions or near artificial implants).

Finite-element modeling (FEM) is widely used to understand the structure–property relationship of materials, and has also been applied in bone mechanics research [30–36]. FEM simulation has proven useful to explain and predict the elastic [33,36], viscoelastic [31,34] and damage [30,35] mechanics in bone. However, FEM simulation of bone and dentin has mostly been performed on the higher levels of the structural hierarchy [30,31,33–36], with only a few simulations at the collagen fibril level [32]; to our knowledge, no FEM studies have focused on viscoelastic behavior of bone at this level. Our recent study [37] showed that the FEM simulations of elastic properties of HAP mineral and collagen phases in bone at the nanoscale matched well with experimental data from corresponding synchrotron measurements. Here, the elastic model is expanded to include viscoelastic properties and interfacial interactions in the FEM simulation to understand and predict the creep behavior of bone subjected to long-term stresses, in conjunction with experimental synchrotron studies of load transfer between HAP mineral and collagen phases.

2. Materials and methods

2.1. Sample preparation

A fresh bovine femur of the posterior leg of a healthy 18 month old Black Angus cow was obtained from a local abattoir (Aurora Packing Company Inc., North Aurora, IL). The bone was cleaned of marrow, stored in gauze soaked with phosphate-buffered saline (PBS) and frozen at $-20\,°C$. After thawing the bone to room temperature, parallel cuts were made perpendicular to the bone long-axis, approximately 5.5 mm apart, with a Buehler Isomet-1000 precision diamond wafering saw. Thereafter, parallel cuts, 4.5 and 3.5 mm apart, respectively, were made in the transverse cross-section of the obtained sample. Parallelepipeds of dimensions $a = 3.0 \pm 0.01$ mm, $b = 4.0 \pm 0.01$ mm and $c = 5.0 \pm 0.01$ mm were obtained, with the c dimension along the longitudinal direction of the femur. All cutting operations were done in deionized water to maintain bone hydration. The two samples used here (labeled 1 and 2) were extracted from adjacent locations at the lateral side of the femur, close to the mid-diaphysis region, with the a dimension parallel to the radial direction (from the bone center to the bone edge) and the b dimension parallel to the bone circumference. After cutting, the samples were weighed with a precision balance and the dimensions were measured with a point micrometer, taking three measurements each time. The samples were then stored in PBS and frozen at $-20\,°C$ until the time of the X-ray experiment.

2.2. X-ray scattering measurements

All the mechanical tests were performed at the 1-ID-C beamline of the Advanced Photon Source (APS) at Argonne National Laboratory. The two samples were thawed to room temperature prior to testing. Uniaxial compressive load was applied with an MTS 858 hydraulic load frame with customized compression platens adapted to maintain the hydration state of the samples during loading, as described previously in Ref. [38]. A small watertight container made of vinyl tubing was attached to the lower platen, which allowed the sample to be fully immersed in PBS. To maintain a constant temperature of 37 °C (designated as body temperature

in the following), the PBS was circulated through the container from a nearby temperature-controlled bath.

Each sample was placed within the sample hydration set-up on the lower compression platen such that the sample was loaded along the bone longitudinal direction with the beam traversing the sample along its smallest dimension. For each sample, an initial wide angle X-ray scattering (WAXS) and small angle X-ray scattering (SAXS) pattern was recorded before mechanical loading. The WAXS pattern, shown in Fig. 1, is obtained from beam interactions with the mineral phase (HAP) of bone. The SAXS pattern (Fig. 1) is a result of X-rays scattering from the regularly spaced HAP platelets within the fibrils (average D-period of 67 nm). Both samples were then loaded in ~10 s to a compressive stress of -80 MPa which was maintained constant for nearly 2 h. Although this high stress is not physiologically relevant over long time scales, it was used here to allow measurable creep strains to accumulate over laboratory time scales. However, these measurements are pertinent in surgical situations where retractors are employed, applying large forces to bones over a period of hours [39]. After loading, WAXS and SAXS diffraction patterns were recorded alternately, with an interval of 85 s between two successive WAXS, and therefore SAXS, measurements. To minimize potential radiation damage, measurements were made over a grid of 20 locations organized in two rows of 10. The two rows were spaced 100 μm apart, 50 μm below and 50 μm above the vertical center of the sample, respectively (Fig. 1). Horizontally neighboring locations were also spaced 100 μm apart, spanning a horizontal range of 500 μm to the left of the horizontal center and 400 μm to the right of the horizontal center when aligned with the direction of the beam. Measurements started in the top left-hand corner of the array traveling first along the horizontal row from left to right and then moving down to measure the locations in the bottom row also from left to right. To obtain measurements for 2 h, the array was measured four times, resulting in a total of 80 measurements per sample, each time starting again with the top leftmost location.

Measurements were taken with a 65.7 keV X-ray beam with a $50 \times 50\ \mu m^2$ cross-section directed at the sample perpendicular to its loading direction. The diffraction patterns were collected
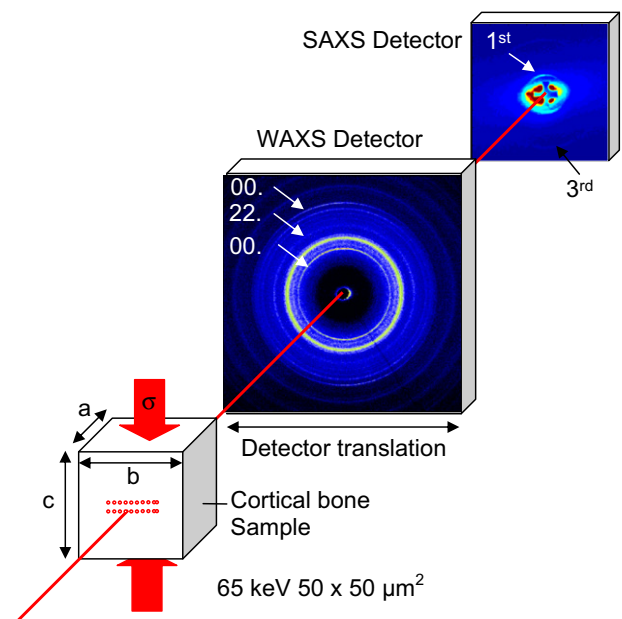
Fig. 1. Schematics of the experimental diffraction set-up showing representative images of the wide- and small-angle X-ray diffraction rings obtained from sample 2 immediately after loading. The circles on the sample represent the 20 sampling locations.

on area detectors placed behind the sample, nominally perpendicular to the direction of the beam. A GE amorphous silicon flat panel detector with a 2048 × 2048 pixel grid and 200 × 200 μm² pixel size, placed at a distance of 1428 mm from the sample, recorded the WAXS patterns which were calibrated by a pressed ceria powder disc (CeO₂, NIST SRM-674a) placed in the beam before and after a measurement series. A Princeton Instruments SCX-TE/CCD with a 1000 × 1000 pixel grid and 22.5 × 22.5 μm² pixel size, placed at a distance of 4050 mm from the sample, recorded the SAXS patterns. To record both the WAXS and SAXS patterns at each location, the GE detector was laterally translated out of the beam direction to expose the CCD camera. The X-ray exposure times were 1 s for each detector. A radiation dose of 0.7 kGy was absorbed by the sampling volume at each measurement of both WAXS and SAXS. Therefore, the accumulated radiation dose at each measurement location, after cycling through the array four times, was 2.8 kGy. This relatively low dose is not expected to significantly affect the mechanical properties of the samples [40–42].

2.3. X-ray scattering analysis

The longitudinal and transverse strains in the mineral and fibrillar phase are calculated as previously discussed in the literature [24,43], with a summary given here. Changes in d-spacing between the lattice planes in the HAP were used to determine elastic strains in the mineral phase, described here as HAP strains. The basic diffraction parameters were first obtained by analyzing the ceria diffraction patterns using the Fit2D software [44]. The parameters determined from this program—beam center, detector tilt and specimen–detector distance—were input in a series of MATLAB programs developed at APS. These programs first convert the WAXS diffraction patterns from radial to Cartesian coordinates. The rings are then fit using a pseudo-Voigt model giving the center of each peak of interest, HAP(00.2), HAP(22.2) and HAP(00.4) in the present case, as a radial distance from the beam center at various azimuthal angles, R(η). The Cartesian plot for radial distance, R(η), vs. azimuth, η, intersect at a single radius for all applied stress levels, called the invariant radius R^*. This stress-free point is used to calculate the orientation-dependent deviatoric strains as $\epsilon(\eta) = (R^* - R(\eta))/R(\eta)$. Strains measured at the azimuthal angles of 90 ± 10° and 270 ± 10° give the longitudinal strain (along the loading direction), while those of 0 ± 10° and 180 ± 10° give the transverse strain.

In the case of the SAXS patterns, well-defined scattering maxima arise from the ∼67 nm D-period of the HAP mineral in the collagen fibrils. In the case of mineralized tissue such as bone and dentin, the primary SAXS contrast associated with these rings is between the relatively dense HAP particles and the collagen phase [45]. Changes in the radii of these SAXS peaks with applied load therefore represent changes in the average HAP particle spacing, which in turn results from cooperative deformation of both the collagen matrix and the HAP particles. Thus, the SAXS-derived strain provides the composite strain at the nanoscale level (without the effects from the larger microstructure such as the osteons), and is referred to here as the fibrillar strain. This fibrillar strain is measured from SAXS rings in a manner similar to the HAP strains from WAXS rings, except that the third-order SAXS ring (corresponding to a D-period of ∼67/3 = 22.3 nm) was only fit over azimuthal ranges of 90 ± 10° and 270 ± 10° due to the preferred longitudinal orientation of the mineralized collagen fibrils, which resulted in incomplete rings. This orientation precluded measurement of the stress-free invariant radius R^* which is instead taken as the value $R^0(\eta = 0)$ when the sample is under zero load. Thus, in contrast to the WAXS data, no information on residual strains in the SAXS data is available.

2.4. Finite-element modeling

A two-dimensional model of the mineralized collagen fibril was subjected to a FEM simulation using the software ABAQUS/ Standard (version 6.10-EF1). The unit cell, shown in Fig. 2, was meshed using quadratic elements (element type CPE8R). Since the diffraction experiments cannot distinguish between intra- and extra-fibrillar HAP effects, the model has been reduced to only the mineralized collagen fibril level with the assumption that all the HAP platelets are intrafibrillar.

The basic geometry of the bone model at the collagen fibril level is based on a previous model used to examine the elastic properties of bone [46], which was originally proposed by Jager and Fratzl [47]. In the unit cell model for elastic properties, the authors took into account the fibrillar structure including the 67 nm D-period of the collagen assembly and the overlapping distribution of HAP platelets in the axial direction. However, this basic geometry ignores interactions between the collagen molecules which are important under creep conditions. Using the previous elastic model as a starting point, a new fibrillar unit cell model is established, as shown in Fig. 2. First, the collagen–HAP intersections are smoothed by tapering the HAP platelets to avoid stress concentration effects. Second, since X-ray dosage was low, the bonding between these two phases is assumed to be perfect in the model. Also, based on the fact that the collagen phase of bone is composed of discrete collagen molecules, which are about 300 nm long and 1.5 nm in effective diameter [48], the previously assumed continuous collagen geometry is modified as follows: because the individual collagen molecule in the axial direction is significantly longer than both the assembly period (∼67 nm) and HAP platelet (mostly <100 nm long in the axial direction), it is improbable that the collagen fibers will terminate exactly at the top or bottom of the mineral plate. Therefore, the formerly continuous collagen matrix is
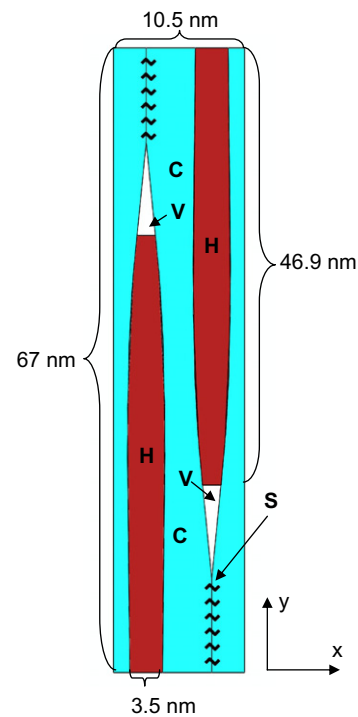
Fig. 2. Geometry of the two-dimensional FEM model for a mineralized collagen fibril, consisting of tapered hydroxyapatite HAP platelets (H) surrounded by a discretized collagen phase (C). Individual collagen blocks (corresponding to the volume of one molecule) are linked with each other through springs (S) and are well bonded to the HAP platelets. The interstitial spaces above and below the HAP platelets are modeled as voids (V).

discretized into several adjacent long collagen blocks, representing individual molecules. To simplify the calculation, only the interfaces between the two collagen blocks directly above or below the platelets are considered, i.e. besides these interfaces, the interactions between collagen molecules are ignored and the collagen is considered as a single phase. This geometry (long molecule and HAP platelet-like shape) implies the presence of a highly hydrated and non-load-bearing region immediately above and below the HAP platelets. In the model, this interstitial space is treated as a void.

As shown in Fig. 2, the interface between adjacent collagen blocks (molecules) is modeled as linked by weak springs to simulate collagen–collagen interactions. Since the strength of the crosslinks between collagen molecules is of the order of covalent bonds [49] whose energy is normally around 420 kJ mol^{-1} [50], and since the crosslink density is about 7.3 mol m^{-3} (based on a $\beta = 25$ case in Ref. [49]), the stiffness of the crosslinks, and therefore the springs in the model, is estimated at 3 MPa; this is the energy per unit volume (product of 420 kJ mol^{-1} and 7.3 mol m^{-3}) which can be viewed as the energy generated by moving a unit area of springs by one unit length.

In the present model, the HAP platelets have a length of 94 nm based on the 50–100 nm range suggested by Ref. [51], a Young's modulus of 114 GPa [52] and a Poisson's ratio of 0.28 [52]. Both the width and the spacing of HAP platelets are taken as 3.5 nm [53]. The collagen phase has a Poisson's ratio of 0.25 [54]. To represent the viscoelastic properties of the collagen phase, an empirical equation proposed by Sasaki et al. [27] for the relaxation modulus of collagen $E(t)$ is used:

$$E(t) = E_0 A_1 \exp[-(t/\tau_1)^\beta] + A_2 \exp(-t/\tau_2), \tag{1}$$

where $E_0 = 5$ GPa is the Young's modulus of collagen (as measured ultrasonically [55]), τ_1 and τ_2 are two relaxation times, β is the stretch exponent on the first term ($0 < \beta \leqslant 1$), and A_1 and A_2 are the weighting fractions of the two terms ($A_1 + A_2 = 1$). Prior research has shown that in most cases, τ_1 and τ_2 span 10–10^3 and 10^4–10^6 s, respectively [16,56,57].

The loading of the model is the same as in the previously described diffraction experiments. A compressive load is applied to the top surface of the unit cell model while the bottom of the unit is fixed in the loading direction and strict periodicity of the unit cell (simulating a volume embedded within a large sample) is maintained in the lateral directions (x direction in Fig. 2). In other words, the lateral displacements for every two nodes of equal height on the two lateral boundaries are assigned to be the same.

The model provides the average HAP strain ε_{HAP} and collagen fibril strain ε_{fib} as a function of time, which can be directly compared to experimental measurements. ε_{HAP} is obtained as the average strain over all the elements in the whole HAP volume (corresponding to average lattice strain in HAP measured by WAXS experimentally); ε_{fib} is taken as the strain of the unit cell, i.e. the displacement of the top of the unit cell divided by the cell height of 67 nm (representing the deformation of the periodic spacing of the HAP mineral in the collagen fibrils, measured by SAXS experimentally) [36]. Since the unit cell is assumed to be representative of the bulk (and thus ignores the presence of any other phases or pores outside of the fibril), the calculated ε_{fib} is assumed to be equal to the macroscopic sample strain (measured experimentally on the sample).

3. Experimental and modeling results

3.1. Scattering results

For the two samples loaded at −80 MPa, Fig. 3 shows the macroscopic creep behavior in a plot of macroscopic strain (calculated
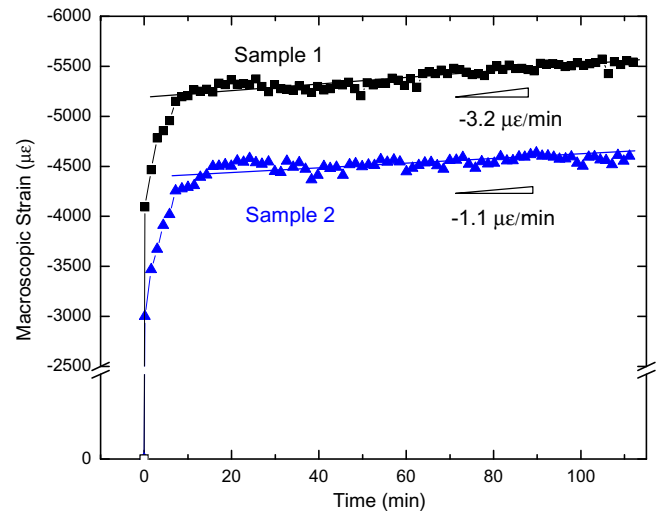
Fig. 3. Plot of the macroscopic strain as a function of time for samples 1 and 2. The sample was loaded to −80 MPa after the first point (hollow symbol) at zero stress. The linear creep rates after the primary creep stage are shown with the corresponding best-fit lines through the data.

from the crosshead displacement and corrected for machine compliance) vs. time. As the stress was ramped to the final value of −80 MPa, the macroscopic sample strain increased rapidly, achieving (mostly) elastic values of −4100 and −3000 με (−0.41% and −0.30%, first solid points in Fig. 3) for samples 1 and 2, respectively, measured 10 s after the maximum stress had been reached. Then, under a constant −80 MPa stress, the sample strain increased in a nonlinear manner for ∼10 min to strain values of approximately −5200 and −4300 με, respectively, corresponding to a primary-like creep region. Finally, the strain accumulated linearly with time until the end of the 2 h experiment, corresponding to a secondary (steady-state) creep period. The macroscopic creep strain rates, defined as the slope of the macroscopic strain vs. time plot in the linear region of Fig. 3, are −3.2 ± 0.2 and −1.1 ± 0.2 με min^{-1} for samples 1 and 2, respectively.

Fig. 4a,b plots all 80 measured HAP elastic strains as a function of creep time. The strain measured in the HAP before loading is −1300 and −1700 με for samples 1 and 2, respectively (first hollow square points in Fig. 4a,b). This residual strain is known to be present in natural bone samples, and may increase crack resistance [23,24]. The initial elastic strain under load, i.e. the first HAP elastic strain measured 10 s after loading, was −3800 and −3700 με for samples 1 and 2, respectively. Thereafter, the HAP elastic strain increases much more slowly in a near-linear fashion with time, at rates of −1.2 ± 0.5 and −1.1 ± 0.4 με min^{-1} for samples 1 and 2 (i.e. at an average rate of −1.2 ± 0.6 με min^{-1}). These strain rates may, however, be affected by spatial variations of the bone mechanical properties due to differences in bone porosity, mineral content or structure [58]. Therefore, by taking X-ray measurements at 20 different locations within each sample to minimize X-ray dose, not only are the effects of creep time on phase strain being measured, but the spatial compositional and structural effects are also assessed. To deconvolute the effect of the creep time and spatial property variations, HAP elastic strain rates were also calculated individually for each of the 20 locations, for which four strain measurements exist at intervals of 28 min (Fig. 4a,b show vertical lines delineating these four cycles). However, due to the small number of measurements taken at each location, the errors on these 20 HAP elastic strain rates are relatively large, averaging 1.3 and 1.0 με min^{-1} for samples 1 and 2, respectively. By taking the average of these 20 slopes measured at each location, the average location-dependent HAP strain rate can be calculated.
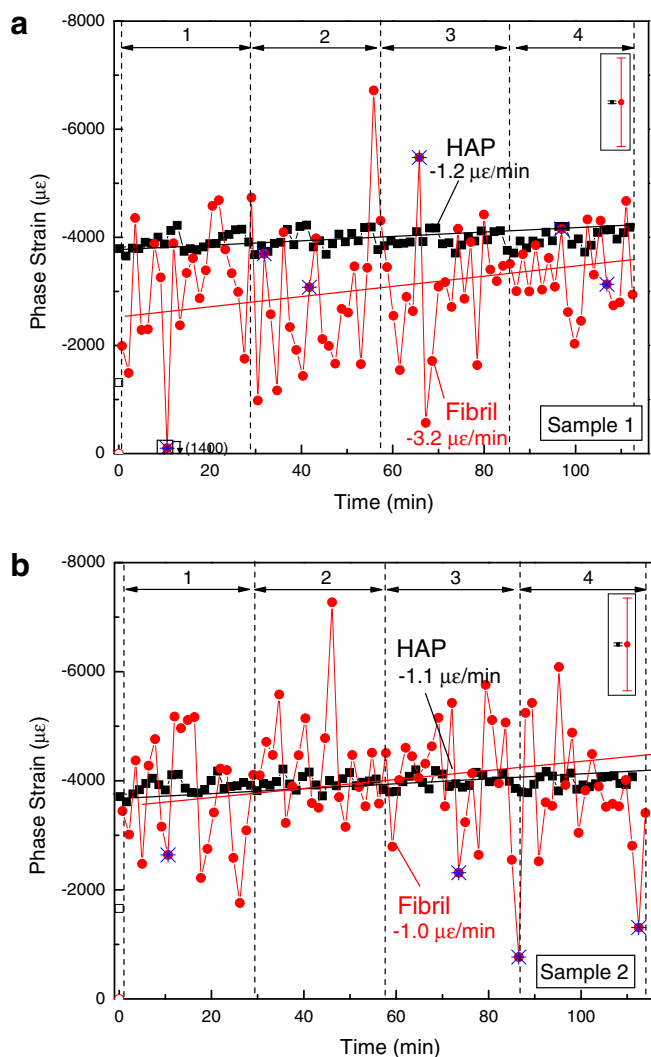
Fig. 4. Plot of elastic HAP and fibrillar strains as a function of time in (a) sample 1 and (b) sample 2. The average errors for the HAP and fibrillar strains are 30 and 840 με, respectively, and are shown by the error bars in the box in the top right-hand corner. The vertical dashed lines delineate the four separate time periods in which the 20 sampling locations were measured under the applied stress. The HAP and fibrillar strain rates are marked next to each linear region, with the corresponding best-fit lines. Fibrillar strain outliers are marked with crosses and were not included in the above best-fits.

For sample 1, the average slope across all 20 locations is -0.4 ± 1.4 με min^{-1}, while for sample 2 it is -0.9 ± 1.0 με min^{-1} (errors are standard deviations), close to the previous values (-3.2 ± 0.2 and -1.1 ± 0.2 με min^{-1}) calculated by using all 80 points.

Due to the short exposure time and relatively weak SAXS peaks, fitting errors for the fibrillar strain measurements were much larger than for HAP strain measurements. To eliminate outliers that may skew the results, any measurement with an error on the ring radius along the loading axis (R(90°) and R(270°)) larger than two standard deviations from the mean error (0.2 pixels from the mean for both samples) were ignored. Out of the 80 measurements taken for each of the samples 1 and 2, only 6 and 4 measurements, respectively, were deemed to be outliers and removed from the data (as shown by crosses in Fig. 4a,b). Even with the increased noise in the fibrillar data which can be seen in Fig. 4a,b, it is apparent that fibrils behave similarly to the HAP particles, i.e. the strain on the fibrils increases very rapidly upon initial loading (elastic strain of ~-2000 με), and then much more slowly and linearly

with continuing time. The fibrillar strain rates, calculated from the slope of all 80 of the strain measurements irrespective of location, are -3.2 ± 3.8 and -1.0 ± 3.5 με min^{-1} in samples 1 and 2, respectively, resulting in an average fibrillar creep rate of -2.1 ± 5.2 με min^{-1}.

Using the same procedure described above to deconvolute the effects of location and creep time, the strain rates at each of the 20 locations were calculated from their four fibrillar strain measurements. Locations that had strain excluded as outlier were not considered. Sample 1, which had 14 usable locations, displayed an average slope of -4.5 ± 14 με min^{-1}. Sample 2, with 16 usable locations, showed an average slope of -1.6 ± 12 με min^{-1}.

3.2. Finite-element modeling results

In the FEM model described above, the matrix behavior is given by Eq. (1) which has four parameters: τ_1, τ_2, β and A_1/A_2. Since τ_1 is between 10 and 10^3 s, the effect of the first term fades away rapidly and the long-term creep behavior is mostly determined by the second term ($\tau_2 > 10^4$ s). The parameters $\tau_1 = 100$ s and $\beta = 1$ [31] were fixed, because of the lack of data in the first several minutes of measurement. Therefore, only two undetermined parameters are left: τ_2 and A_1/A_2. To determine these two parameters, the average creep rates of both the mineral and fibrillar phases obtained by simulation were fit to the average corresponding strain rates from the two samples as measured experimentally by WAXS and SAXS ($d\varepsilon_{HAP}/dt = -1.2 \pm 0.6$ με min^{-1} and $d\varepsilon_{fib}/dt = -2.1 \pm 5.2$ με min^{-1}). By using the fact that the collagen modulus at long times (in the mechanical measurement range) is about 1 GPa [51], a reasonable fit to the experimental HAP and fibrillar creep rates is obtained for $\tau_2 = 10^5$ s and $A_1/A_2 = 6$. Both of these values are well within the accepted range [31].

The simulated phase strain vs. time curve and fitted relaxation modulus of collagen phase are shown in Fig. 5. These best-fit parameters generated $d\varepsilon_{HAP}/dt = -0.9$ με min^{-1} and $d\varepsilon_{fib}/dt = -2.1$ με min^{-1}, which are in the error range of the experimental average HAP strain rate of -1.2 ± 0.6 με min^{-1} and average fibrillar creep rate of -2.1 ± 5.2 με min^{-1} (which is also very close to average macroscopic creep rate -2.2 ± 0.3 με min^{-1}). The model also captures the lack of a primary creep region for the HAP strain. However, the model shows a primary-like creep region for the fibrillar strain which is not observed in the SAXS strain data. The initial HAP strain due to elastic loading obtained from the model is about -3100 με (sum of -1600 με from the applied stress calculated in the model and -1500 με, the average residual strain determined experimentally), which is in general agreement with the experimental value of -3700 με. The fibrillar strain in the post-primary creep zone obtained from the model is about -5000 με, which is in agreement with macroscopic measurement value (~-5000 με) but larger than the SAXS measurement value (~-2000 με). The von Mises stress evolution in the unit cell model during the creep simulation, for an applied stress of -80 MPa, is shown in Fig. 6. It is apparent that the stress in the collagen phase is being transferred to the mineral phase during the creep process in the first 20 min of the experiment. Beyond that time, no significant evolution can be observed in the contour plot of von Mises stress (Fig. 6). The average von Mises stress in the collagen phase decreases from 18 MPa (in the initial elastic state, just after loading) to 14 MPa (in the final state after 2 h of creep), while the average von Mises stress in the HAP phase increases from 179 to 192 MPa.

4. Discussion

Only two samples were subjected to creep experiments due to the limited access to synchrotron beam time and given the
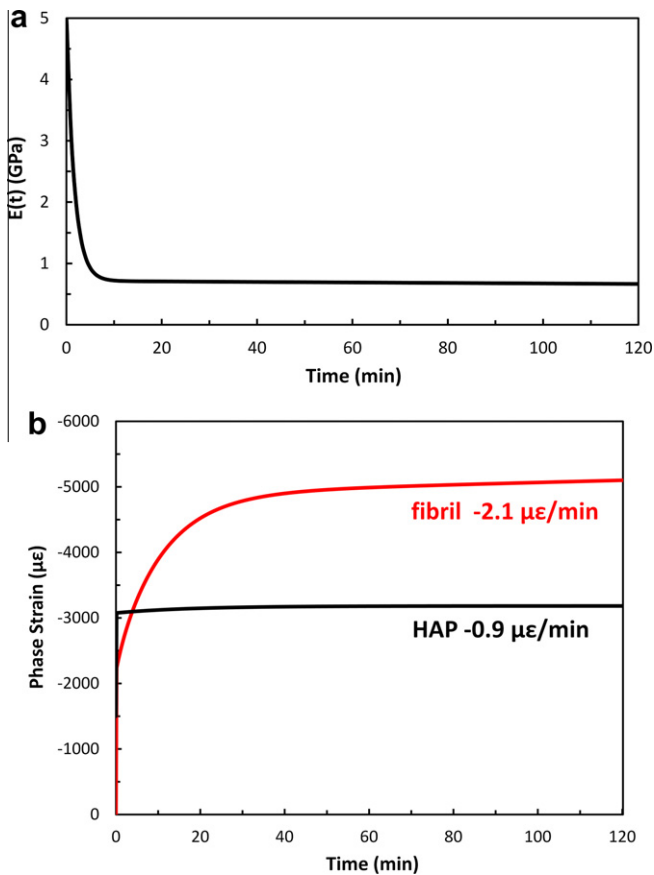
Fig. 5. (a) Plot of collagen relaxation modulus vs. time (Eq. 1) using the parameters obtained from fitting the experimental data. (b) Plot of average HAP and fibrillar strains as a function of creep time at -80 MPa as determined by FEM calculations (-1500 με is added to the HAP strain curve due to residual strain in the mineral phase).

exploratory nature of these novel experiments, whose goal was to identify mechanisms, rather than provide high-precision creep data with statistically determined error bars. While this pair of samples illustrates the level of reproducibility within neighboring positions in a bone, future large-scale, multi-sample experiments will be needed to quantify reproducibility across various animals, and for various regions in a femur in a given animal.

4.1. X-ray scattering

The average experimental macroscopic creep strain rate of the bone samples, -2.2 ± 0.3 με min^{-1} (Fig. 3), is of the same order as room temperature steady-state creep rates in bovine cortical bone of -9.7 and -1.0 με min^{-1}, calculated from the empirical equations derived from experimental measurements by Fondrk et al. (over 25–120 MPa) [59] and Rimnac et al. (over 71–115 MPa) [15], as modified by Bowman et al. [14].

The magnitude of the fibrillar strain is lower than expected, with elastic strain values below that of the HAP platelets. This results from the lack of an accurate invariant stress point for the fibrillar measurements. All of the fibrillar strain values are calculated in relation to the D-period measured at no load. Error in this initial measurement causes a shift in the rest of the fibrillar strains. Therefore although the magnitude of the fibrillar strain may not be accurate, the relative evolution with time is correct.

The fibrillar strain (Fig. 4a,b) shows an increase with increasing creep time. This is expected, as the fibrillar strain represents the cooperative deformation of the HAP and collagen (and therefore

of the mineralized fibril strain) which is anticipated to scale directly with the average macroscopic strain. This is because the sampled mineralized fibrils are aligned with the loading direction and compose the bulk of the bone sample, which is itself accumulating compressive strain along the loading axis with increasing time. The fibrillar creep is a measure of the bone composite creep without accounting for macroscopic structures such as osteons or porosity. Therefore the near identical values obtained for the macroscopic and fibrillar strain rates suggest that bovine cortical bone creep rate is controlled by fibrillar deformation rather than other larger-scale deformation mechanisms such as lamellae sliding or the collapse of porosity.

Both the overall and point-dependent HAP strain rates, which were within error of each other, showed an increase in HAP elastic strain with increasing creep time. Since pure HAP is not expected to undergo significant creep (plastic) strain at these experimental stresses and temperatures, this time-dependent HAP strain is elastic and associated with load transfer from the viscoelastically deforming collagen. This increase in HAP elastic strain is expected given the composite structure of bone consisting of a collagen matrix with discontinuous, reinforcing HAP platelets. In nonbiological composites, load is transferred from the creeping matrix phase to the elastic reinforcement with increasing creep time, causing an increase in elastic strain in the latter phase [60–62]. Here, the same process is taking place: the more compliant, viscoelastically creeping collagen matrix transfers load to the stiffer, purely elastic HAP platelets, causing an increase in the HAP elastic strain with time, even though the HAP alone has no time-dependent response.

The small differences between the overall and point-dependent HAP strain rates, suggests that there is little variability in the mechanical properties between the different sampling locations in the samples. The properties of bone are known to vary with location, e.g. due to the presence of osteonal bone which is less stiff (by 4–17%) than the surrounding interstitial bone [63–65]. Thus, if the X-ray beam samples more osteons in a given location, higher elastic strains may be measured. However, given the approximately random arrangement of osteons in bone, the sampling volume of each 50 μm × 50 μm × 3 mm location should include 10–15 osteons (200–300 μm in diameter), minimizing the intra-sample variability. The large errors on the fibrillar point-dependent strain rates are not due to intra-sample variations, but to experimental errors associated with the variability of the diffraction data shown in Fig. 4. This variability is due to the low irradiation exposure times needed to minimize damage to the bone samples that also result in low signal-to-noise ratios for the SAX scattering peaks, making strain analysis more difficult.

Even with experimental error, the average strain rate of the HAP (-1.2 ± 0.6 με min^{-1}) and the fibrils (-2.1 ± 5.2 με min^{-1}) are similar in magnitude. This suggests that, in cortical bone, collagen is able to transfer load to the HAP very efficiently, thus requiring a strong interface between the two phases. This close correlation between the strain rates also suggests that, for the creep times studied here, the creep rate of bone is not controlled only by the collagen or the HAP crystallites but by the cooperative deformation of both. Macroscopic creep deformation can also accrue by damage at the HAP/collagen interface, a case that is not considered here.

4.2. Finite-element modeling

Despite its many simplifications, the present two-dimensional mineralized collagen fibril model (Fig. 2) successfully reproduces the experimental phase and sample strain rates with two adjustable parameters, both of which take physically credible values. In the model, the bonding between the collagen and mineral phases is assumed to be perfect. This assumption is based on the fact that the X-ray dose for the measurement is relatively low, which will
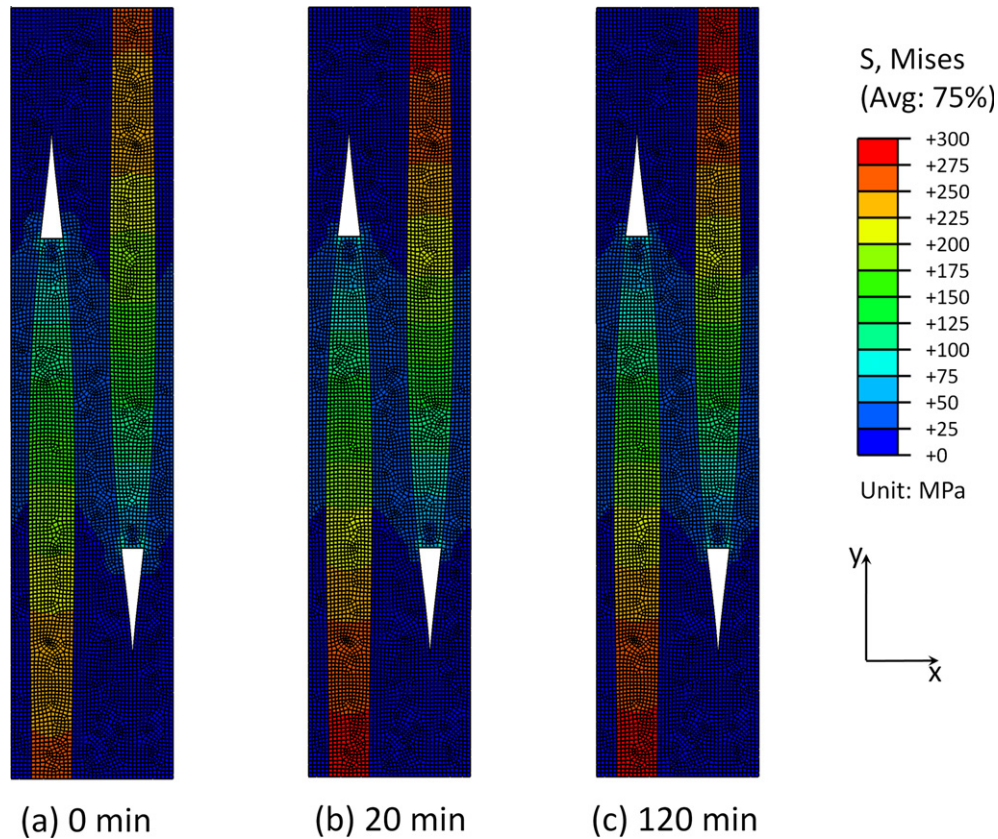
Fig. 6. Von Mises stress contour plot of the FEM unit cell model during creep under an applied stress of −80 MPa: (a) immediately upon loading (t = 0), (b) t = 20 min, (c) final state (t = 120 min).

cause little damage to the mineral–collagen interface [66]. A well-bonded interface between the two phases enables load to be efficiently transferred from the collagen to the HAP platelets. In the current model with no debonding (i.e. no sliding between collagen and mineral phases), any separation between adjacent collagen blocks (molecules) should also be limited. This is confirmed in the model, as varying the spring stiffness values between 1 and 50 MPa has very little effect on the predicted creep rates. While relative slipping of neighboring collagen blocks (molecules) was not considered directly in the model, this effect can be extracted from the viscoelastic properties of collagen phase. The viscoelastic properties of collagen phase has contributions from two different mechanisms [31]: (i) molecular contraction, which has a shorter relaxation time (the first term in Eq. (1)); and (ii) molecular slippage, which has a longer relaxation time (the second term in Eq. (1)). From the simulation results, the slippage mechanism provides only a small contribution to the viscoelasticity of collagen phase ($A_2/A_1 = 1/6$, i.e. a seventh of the total strain is due to slippage), under the stress considered here. Sasaki et al. [27] reported that the slippage effect between collagen molecules becomes significant when a tensile stress applied on a bovine tendon is larger than 8 MPa. While the magnitude of the stress in this study is higher (−80 MPa), it is compressive and it is applied on mineralized bovine bone where the mineral platelets bear most of the stress, so the effective stress on the collagen phase is smaller than the applied stress. In fact, once creep reaches a steady state, the average von Mises stress calculated in the collagen phase is below 15 MPa, which is of the same order as the critical value determined by Sasaki et al. [27]. Therefore, the assumption that slipping between collagen molecules does not occur in our samples is credible.

A comparison of the shape of the macroscopic strain curve (Fig. 3), the experimental phase strain curves (Fig. 4) and the modeling strain curves (Fig. 5) provides insights about how the composite creep behavior differs from the phase creep behaviors. In Fig. 3, there is a clear presence of primary nonlinear creep in the first ∼10 min after loading. During that same time period, the experimental phase strains also increase, though purely linearly (Fig. 4). The FEM simulation (Fig. 5) accurately predicts the lack of primary creep in the HAP strains, but shows nonlinear creep for the fibrils after initial loading. This discrepancy is probably caused by the large errors and small number of measurements in the fibrillar strain over the first 10 min of deformation. The scatter in these measurements may be concealing a zone of primary creep.

It is important to recognize the limitations of the simulation work. Since the simulation work is done by FEM, which is based on continuum mechanics, but the unit cell model is at the nanoscale, three key assumptions of the simulation work and their influence on the simulation results must be addressed. First, it is assumed that the Young's modulus of the mineral platelets is the same as that reported for bulk crystalline HAP. However, the mineral platelets are very thin in natural mineralized collagen fibrils, in most of the cases less than 5 nm [53]. Based on the crystal structure of HAP [67], there are only a few unit cells in the thickness direction of the platelets. Studies have shown that the outer layer of mineral platelets is amorphous [68]; therefore, the large surface-area-to-volume ratio of the platelets can significantly change their properties. By using a simplified core–shell model, the overall modulus of the mineral platelets can be depressed to values as low as 95 GPa [37] (compared with 114 GPa used in the current simulation). To address this effect, the unit cell model can be applied but with this modified modulus of mineral phase. Second, the properties of the collagen phase in bone are assumed to be homogeneous and isotropic, which may, however, be incorrect due to the complex nanoscale structure of the collagen phase

and constrained volume effects (e.g. collagen molecules above mineral platelets vs. collagen molecules between mineral platelets). This problem is partially solved by considering the complex structure in the model (see Fig. 2), and further relieved by the simulation results showing that the interactions between collagen molecules contribute weakly to the viscoelastic properties of the collagen phase. In fact, the equation proposed by Sasaki et al. applies to both tendon (which has a relatively homogeneous structure) and bone cases, but with different parameters [16,18,27,56]. The choice of parameters in the equation can provide the equivalent overall properties of the collagen phase. Third, the bonding between the collagen and mineral phases is assumed to be perfect. This is based on the fact that, in the experiment, both X-ray irradiation dosage (2.8 kGy) and mechanical loading (-80 MPa) are relatively small. However, with the combination of the above two effects and the stress concentration effect, debonding might occur on a small portion of the interfaces between the two phases. However, as long as most of the interface is bonded, the load can be transferred from the collagen to the mineral phase, as in a synthetic platelet-reinforced composite. Thus, we believe that the unit cell model captures the major mechanisms active during the creep of bone samples.

5. Conclusions

The viscoelastic strain at the fibrillar level and the associated time-dependent load transfer from collagen to HAP platelets were measured in bone for the first time, using a combination of wide- and small-angle synchrotron X-ray scattering. For bovine cortical bone subjected to a compressive stress of -80 MPa, compressive strain measured macroscopically on the whole sample accumulates near linearly with time after an initial period of nonlinear strain accumulation. In the linear region, strain measured macroscopically over the whole sample accumulates at a similar rate as strain measured at the nanoscale by synchrotron X-ray diffraction at the fibrillar level, which encompasses the elastic deformation of the HAP platelets as well as the viscoelastic deformation of the surrounding collagen fibers within the fibril. Furthermore, the rate of accumulation of elastic strain in the HAP platelets is similar to the fibrillar strain rate, indicating that load is being continuously shed from the creeping protein matrix to the elastic HAP platelets, as previously reported for many nonbiological composites, and implying a well-bonded interface. Finite-element modeling confirms this hypothesis, by showing that increases in the HAP and fibrillar strain rates of the same magnitude as measured by X-ray diffraction can be obtained for the HAP and the mineralized fibrils when the two phases are well bonded.

Acknowledgments

Appendix A. Figures with essential colour discrimination

Certain figures in this article, particularly Figures 1–6, are difficult to interpret in black and white. The full colour images can be found in the on-line version, at doi:10.1016/j.actbio.2011.08.014.

References

[1] Weiner S, Wagner HD. The material bone: structure mechanical function relations. Ann Rev Mater Res 1998;28:271–98.
[2] Chen PY, Stokes AG, McKittrick J. Comparison of the structure and mechanical properties of bovine femur bone and antler of the North American elk (Cervus elaphus canadensis). Acta Biomater 2009;5:693–706.
[3] Bowman SM, Keaveny TM, Gibson LJ, Hayes WC, McMahon TA. Compressive creep-behavior of bovine trabecular bone. J Biomech 1994;27:301–10.
[4] Walsh WR, Guzelsu N. Compressive properties of cortical bone–mineral organic interfacial bonding. Biomaterials 1994;15:137–45.
[5] Evans FG, Vincente R. Relations of compressive properties of human cortical bone to histological structure, calcification. J Biomech 1974;7:1.
[6] Bonfield W, Tully AE. Ultrasonic analysis of the Young modulus of cortical bone. J Biomed Eng 1982;4:23–7.
[7] Rho JY, Ashman RB, Turner CH. Youngs modulus of trabecular and cortical bone material—ultrasonic and microtensile measurements. J Biomech 1993;26:111–9.
[8] Dechow PC, Nail GA, Schwartzdabney CL, Ashman RB. Elastic properties of human supraorbital and mandibular bone. Am J Phys Anthropol 1993;90:291–306.
[9] Bembey AK, Bushby AJ, Boyde A, Ferguson VL, Oyen ML. Hydration effects on the micro-mechanical properties of bone. J Mater Res 2006;21:1962–8.
[10] Bembey AK, Oyen ML, Bushby AJ, Boyde A. Viscoelastic properties of bone as a function of hydration state determined by nanoindentation. Philos Mag 2006;86:5691–703.
[11] Rho JY, Tsui TY, Pharr GM. Elastic properties of human cortical and trabecular lamellar bone measured by nanoindentation. Biomaterials 1997;18:1325–30.
[12] Rho JY, Roy ME, Tsui TY, Pharr GM. Elastic properties of microstructural components of human bone tissue as measured by nanoindentation. J Biomed Mater Res 1999;45:48–54.
[13] Yamashita J, Li X, Furman BR, Rawls HR, Wang X, Agrawal CM. Collagen and bone viscoelasticity: a dynamic mechanical analysis. J Biomed Mater Res 2002;63:31–6.
[14] Bowman SM, Gibson LJ, Hayes WC, McMahon TA. Results from demineralized bone creep tests suggest that collagen is responsible for the creep behavior of bone. J Biomech Eng 1999;121:253–8.
[15] Rimnac CM, Petko AA, Santner TJ, Wright TM. The effect of temperature, stress and microstructure on the creep of compact bovine bone. J Biomech 1993;26:219–28.
[16] Sasaki N, Nakayama Y, Yoshikawa M, Enyo A. Stress-relaxation function of bone and bone-collagen. J Biomech 1993;26:1369–76.
[17] Folkhard W, Mosler E, Geercken W, Knorzer E, Nemetschekgansler H, Nemetschek T, et al. Quantitative-analysis of the molecular sliding mechanism in native tendon collagen—time-resolved dynamic studies using synchrotron radiation. Int J Biol Macromol 1987;9:169–75.
[18] Sasaki N, Odajima S. Elongation mechanism of collagen fibrils and force–strain relations of tendon at each level of structural hierarchy. J Biomech 1996;29:1131–6.
[19] Balch DK, Dunand DC. Load partitioning between ferrite and cementite during elasto-plastic deformation of an ultrahigh-carbon steel. Acta mater 2007;55:1999–2011.
[20] Mueller R, Rossoll A, Weber L, Bourke MAM, Dunand DC, Mortensen A. Tensile flow stress of ceramic particle-reinforced metal in the presence of particle cracking. Acta mater 2008;56:4402–16.
[21] Young ML, DeFouw JD, Almer DC, Dunand. Load partitioning during compressive loading of a Mg/MgB$_2$ composite. Acta Mater 2007;55:3467–78.
[22] Akhtar R, Daymond MR, Almer JD, Mummery PM. Load transfer in bovine plexiform bone determined by synchrotron X-ray diffraction. J Mater Res 2008;23:543–50.
[23] Almer JD, Stock SR. Internal strains and stresses measured in cortical bone via high-energy X-ray diffraction. J Struct Biol 2005;152:14–27.
[24] Almer JD, Stock SR. Micromechanical response of mineral and collagen phases in bone. J Struct Biol 2007;157:365–70.
[25] Gupta HS, Seto J, Wagermaier W, Zaslansky P, Boesecke P, Fratzl P. Cooperative deformation of mineral and collagen in bone at the nanoscale. PNAS 2006;103:17741–6.
[26] Borsato KS, Sasaki N. Measurement of partition of stress between mineral and collagen phases in bone using X-ray diffraction techniques. J Biomech 1997;30:955–7.
[27] Sasaki N, Shukunami N, Matsushima N, Izumi Y. Time-resolved X-ray diffraction from tendon collagen during creep using synchrotron radiation. J Biomech 1999;32:285–92.
[28] Puxkandl R, Zizak I, Paris O, Keckes J, Tesch W, Bernstorff S, et al. Viscoelastic properties of collagen: synchrotron radiation investigations and structural model. Philos Trans R Soc Lond Ser B-Biol Sci 2002;357:191–7.
[29] Gupta HS, Seto J, Krauss S, Boesecke P, Screen HRC. In situ multi-level analysis of viscoelastic deformation mechanisms in tendon collagen. J Struct Biol 2010;169:183–91.
[30] Borah B, Gross GJ, Dufresne TE, Smith TS, Cockman MD, Chmielewski PA, et al. Three-dimensional microimaging (MRμI and μCT), finite element modeling, and rapid prototyping provide unique insights into bone architecture in osteoporosis. The Anat Rec 2001;265:101–10.

[31] Cherraf-Schweyer C, Maurice G, Taghite M, Taous K. An experimental and theoretical approach of elasticity and viscoelasticity of compact and sponge bone with periodic homogenization. Comp Meth Biomech Biomed Eng 2007;10:195–207.

[32] Gao HJ, Ji BH, Jäger IL, Artz E, Fratzl P. Materials become insensitive to flaws at nanoscale: lessons from nature. PNAS 2003;100:5597–600.

[33] Hara T, Tanck E, Homminga J, Huiskes R. The influence of microcomputed tomography threshold variations on the assessment of structural and mechanical trabecular bone properties. Bone 2002;31:107–9.

[34] Natali AN, Carniel EL, Pavan PG. Constitutive modelling of inelastic behaviour of cortical bone. Med Eng Phys 2008;30:905–12.

[35] Stolken JS, Kinney JH. On the important of geometric nonlinearity in finite-element simulations of trabecular bone failure. Bone 2003;33:494–504.

[36] Verhulp E, van Rietbergen B, Huiskes R. Comparison of micro-level and continuum-level voxel models of the proximal femur. J Biomech 2006;39:2951–7.

[37] Yuan F, Stock S, Haeffner D, Almer J, Dunand D, Brinson L. A new model to simulate the elastic properties of mineralized collagen fibril. Biomech Model Mechanobiol 10:147–60.

[38] Deymier-Black AC, Almer JD, Haeffner DR, Dunand DC. Effect of freeze-thaw cycles on load transfer between the biomineral and collagen phases in bovine dentin. Mater Sci Eng, C 2010 (under review).

[39] Bolotin G, Buckner GD, Campbell NB, Kocherginsky M, Raman J, Jeevanandam V, et al. Tissue-disruptive forces during median sternotomy. Heart Surg Forum 2007;10:E487–92.

[40] Barth HD, Launey ME, MacDowell AA, Ager JW, Ritchie RO. On the effect of X-ray irradiation on the deformation and fracture behavior of human cortical bone. Bone 2010;46:1475–85.

[41] Nguyen H, Morgan DAF, Forwood MR. Sterilization of allograft bone: effects of gamma irradiation on allograft biology and biomechanics. Cell Tissue Bank 2007;8:93–105.

[42] Singhal A, Deymier-Black AC, Almer JD, Dunand DC. Effect of high-energy X-rays doses on bone elastic properties and residual strains. J Mech Behav Biomed Mater 2011; doi: 10.1016/j.jmbbm.2011.05.035.

[43] Deymier-Black AC, Almer JD, Stock SR, Haeffner DR, Dunand DC. Synchrotron X-ray diffraction study of load partitioning during elastic deformation of bovine dentin. Acta Biomater 2010;6:2172–80.

[44] Hammersley AP. FIT2D V9.129 reference manual V3.1. ESRF98HA01T. ESRF Internal Report, 1998.

[45] Fratzl P, Schreiber S, Klaushofer K. Bone mineralization as studied by small-angle X-ray scattering. Connect Tissue Res 1996;35:9–16.

[46] Yuan F, Stock SR, Haeffner DR, Almer JD, Dunand DC, Brinson LC. A new model to simulate the elastic properties of mineralized collagen fibril. Biomech Model Mechanobiol 2011;10:147–60.

[47] Jager I, Fratzl P. Mineralized collagen fibrils: a mechanical model with a staggered arrangement of mineral particles. Biophys J 2000;79:1737–46.

[48] Orgel JPRO, Miller A, Irving TC, Fischetti RF, Hammersley AP, Wess TJ. The in situ supermolecular structure of type I collagen. Structure 2001;9:1061–9.

[49] Buehler MJ. Nanomechanics of collagen fibrils under varying cross-link densities: atomistic and continuum studies. J Mech Behav Biomed Mater I 2008:59–67.

[50] Cottrell TL. The strengths of chemical bonds, 2nd ed.. London: Butterworths; 1958.

[51] Ascenzi A, Bonucci E, Bocciare Ds. An electron microscope study of osteon calcification. J Ultrastruct Res 1965;12:287.

[52] Gilmore RS, Katz JL. Elastic properties of apatites. J Mater Sci 1982;17:1131–41.

[53] Lowenstam HA, Weiner S. On biomineralization. New York: Oxford University Press; 1989.

[54] Meyers MA, Chen PY, Lin AYM, Seki Y. Biological materials: structure and mechanical properties. Prog Mater Sci 2008:1–206.

[55] Chapel' V, Lavrent'ev V. Piezoelectric effect in collagen structures. Mech Comp Mater 1987;14:574–9.

[56] Sasaki N, Odajima S. Stress–strain curve and Young's modulus of a collagen molecule as determined by the X-ray diffraction technique. J Biomech 1996;29:655–8.

[57] Sasaki N, Enyo A. Viscoelastic properties of bone as a function of water-content. J Biomech 1995;28:809–15.

[58] Carter DR, Spengler DM. Mechanical-properties and composition of cortical bone. Clin Orthop Rel Res 1978:192–217.

[59] Fondrk M, Bahniuk E, Davy DT, Michaels C. Some visco–plastic characteristics of bovine and human cortical bone. J Biomech 1988;21:623–30.

[60] Daymond M, Lund C, Bourke M, Dunand D. Elastic phase-strain distribution in a particulate-reinforced metal-matrix composite deforming by slip or creep. Metallurg Mater Trans A 1999;30:2989–97.

[61] Madgwick A, Mori T, Withers PJ. A neutron diffraction study of creep and damage occurrence in an A359/SiC composite. Mater Sci Eng A-Struct Mater Prop Microstruct Process 2002;333:232–8.

[62] Winand HMA, Whitehouse AF, Withers PJ. An investigation of the isothermal creep response of Al-based composites by neutron diffraction. Mater Sci Eng A-Struct Mater Prop Microstruct Process 2000;284:103–13.

[63] Hoffler CE, Guo XE, Zysset PK, Goldstein SA. An application of nanoindentation technique to measure bone tissue lamellae properties. Trans ASME 2005;127.

[64] Rho JY, Zioupos P, Currey JD, Pharr GM. Microstructural elasticity and regional heterogeneity in human femoral bone of various ages examined by nanoindentation. J Biomech 2002;35:189–98.

[65] Rho J-Y, Roy II ME, Tsui TY, Pharr GM. Elastic properties of microstructural components of human bone tissue as measured by nanoindentation. J Biomed Mat Res-A 1999;45.

[66] Hubner W, Blume A, Pushjakova R, Dekhtyar Y, Hein HJ. The influence of X-ray radiation on the mineral/organic matrix interaction of bone tissue: an FT-IR microscopic investigation. Int J Artif Organs 2005;28:66–73.

[67] Matsunaga K, Kuwabara A. First-principles study of vacancy in hydroxyapatite. Phys Rev B 2007; 014102.

[68] Olszta MJ, Cheng XG, Jee SS, Kumar R, Kim YY, Kaufman MJ, et al. Bone structure and formation: a new perspective. Mater Sci Eng R Rep 2007;58:77–116.